DOI: 10.1002/ (adfm.201605413R1)
Article type: Full Paper

Evidence and effect of photogenerated charge transfer for enhanced photocatalysis in WO_3/TiO_2 heterojunction films: a computational and experimental study.

Carlos Sotelo-Vazquez[1], Raul Quesada-Cabrera[1], Min Ling[1], David O. Scanlon[1,2], Andreas Kafizas[1], Pardeep Kumar Thakur[2], Tien-Lin Lee[2], Alaric Taylor[3], Graeme W. Watson[4], Robert G. Palgrave[1], James R. Durrant[5], Christopher S. Blackman[1], and Ivan P. Parkin[1]**

Mr. C. Sotelo-Vazquez, Dr. Raul Quesada-Cabrera, Mr. Min Ling, Dr. D. O. Scanlon, Dr. A. Kafizas, Dr. R. G. Palgrave, Dr. C. S. Blackman, Prof. I. P. Parkin
University College London, Department of Chemistry, 20 Gordon St., London WC1H 0AJ (United Kingdom).
E-mail: (i.p.parkin@ucl.ac.uk; r.quesada@ucl.ac.uk)
Dr. D. O. Scanlon, Dr. P. K. Thakur, Dr. T-L. Lee
Diamond Light Source Ltd., Harwell Science and Innovation Campus, Didcot, OX11 0DE (United Kingdom).
Mr. Alaric Taylor
University College London, Department of Electronic & Electrical Engineering, Torrington Place, London, WC1E 7JE (United Kingdom).
Prof. G. W. Watson
Trinity College Dublin, School of Chemistry and CRANN Institute, Dublin 2, Ireland.
Prof. J. R. Durrant
Department of Chemistry, Imperial College London, Exhibition Road, London SW7 2AZ (United Kingdom).

Keywords: (titanium dioxide, tungsten trioxide, heterojunction, band alignment, density functional theory, hard X-ray photoelectron spectroscopy, transient absorption spectroscopy, photocatalysis)

(Abstract: Semiconductor heterojunctions are used in a wide range of applications including catalysis, sensors and solar-to-chemical energy conversion devices. These materials can spatially separate photogenerated charge across the heterojunction boundary, inhibiting recombination processes and synergistically enhance their performance beyond the individual components. In this work, we investigate the WO_3/TiO_2 heterojunction grown by chemical vapour deposition. This consisted of a highly nanostructured WO_3 layer, of vertically aligned nanorods, that was coated then with a conformal layer of TiO_2. This heterojunction showed an

unusual electron transfer process, where photogenerated electrons moved from the WO_3 layer into TiO_2. State-of-the-art hybrid density functional theory and hard X-ray photoelectron spectroscopy were used to elucidate the electronic interaction at the WO_3/TiO_2 interface. Transient absorption spectroscopy showed that recombination was substantially reduced, extending both the lifetime and population of photogenerated charges into timescales relevant to most photocatalytic processes. This increased the photocatalytic efficiency of the material, which is among the highest ever reported for a thin film. In allying computational and experimental methods, we believe this is an ideal strategy for determining the band alignment in metal oxide heterojunction systems.)

1. Introduction

Heterojunction materials may benefit from charge transfer processes by coupling two semiconductors with appropriate band structures in order to drive a particular functionality. This phenomenon has been used advantageously in photovoltaics technologies as well as in organic and dye-sensitized solar cells[1] and more recently in the field of photocatalysis, in particular for water-splitting applications.[2] In a heterojunction, the band structures of the two coupled semiconductors may align favourably so as to encourage migration of photogenerated electrons (e^-) and holes (h^+) in separate directions across the heterojunction boundary. This vectorial separation reduces electron-hole recombination, and when used in photocatalytic systems, can enhance their efficiency.[3–5] A remarkable example is the ubiquitous commercial TiO_2 P25 (*Evonik*, formerly *Degussa*), which consists of a ~ 3:1 ratio of anatase (E_{bg}= 3.20 eV) and rutile (E_{bg}= 3.00 eV) and is considered the benchmark photocatalyst.[6] This heterojunction material, as well as many other successful systems such as Cu_2O/TiO_2,[7] $WO_3/BiVO_4$,[8] or $ZnO/BiVO_4$,[9] have shown a clear enhancement in their photoresponse compared to that of their individual analogues.

The synergistic interaction between different semiconductor phases strongly depends on the synthesis method and the physical properties of the resulting materials (particle size and shape, film thickness, specific surface area, crystallinity, etc.).[5] It is important to note that a particular charge transfer direction should not be *assumed* solely on the grounds of band alignment. In fact, structural defects at the interface of two dissimilar phases may hamper or even reverse the expected electron transfer between them.[10] For P25, it has been generally accepted that rutile acts as an electron sink in the anatase-rutile system.[11] It has been assumed that an increased population of positive holes (h^+) on the anatase side promotes the formation of hydroxyl radicals, which in turn participate in oxidation reactions at the catalyst surface and hence enhance the activity of the material. However, recent computational and experimental evidence[3,4,11] has suggested an oppositely staggered band alignment, where electrons transfer from rutile to anatase. The traditional observation of rutile as an electron sink may then be explained by the presence of deep electron trap states at the heterojunction interface, which can reverse the direction of charge transfer.

Heterojunction WO_3/TiO_2 materials have been widely employed in photocatalysis, showing a clear enhancement of their photoresponse upon ultraviolet irradiation.[12–14] In these systems, electron transfer from TiO_2 (E_{bg} = 3.20 eV) to WO_3 (E_{bg} = 2.74 eV) is often inferred from a colour change in WO_3 from yellow to blue upon photo-excitation. The colour change is due to the formation of blue polarons (W^{5+}) upon reduction of W^{6+} ions, as evidenced by X-ray photoelectron spectroscopy (XPS).[15] This charge transfer has been widely reported[12,14,16] and correlates with the band alignment represented in Figure 1A. However, as we demonstrate in this work, it is possible to engineer a WO_3/TiO_2 system where electrons transfer from WO_3 to TiO_2, according to the band alignment illustrated in Figure 1B. Herein, we have developed a nanostructured WO_3/TiO_2 film using chemical vapour deposition methods, consisting of WO_3 nanorods of monoclinic structure, highly oriented in the [002] plane, coated with a thin

conformal layer of anatase TiO_2. Contrary to widely reported observation, our WO_3/TiO_2 heterojunctions preserved their original colour and did not show any evidence of reduced tungsten species upon photoexcitation. Remarkably, our WO_3/TiO_2 heterojunctions showed record high photocatalytic activity in the degradation of a model organic pollutant. State-of-the-art hybrid density functional theory (DFT), hard X-ray photoelectron spectroscopy (HAXPES) and transient absorption spectroscopy (TAS) were combined to investigate the band alignment of our WO_3/TiO_2 heterojunction and explain its outstanding photocatalytic activity. By allying such computational and experimental methods, we consider our approach a general strategy for determining the band alignment in metal oxide heterojunction systems.

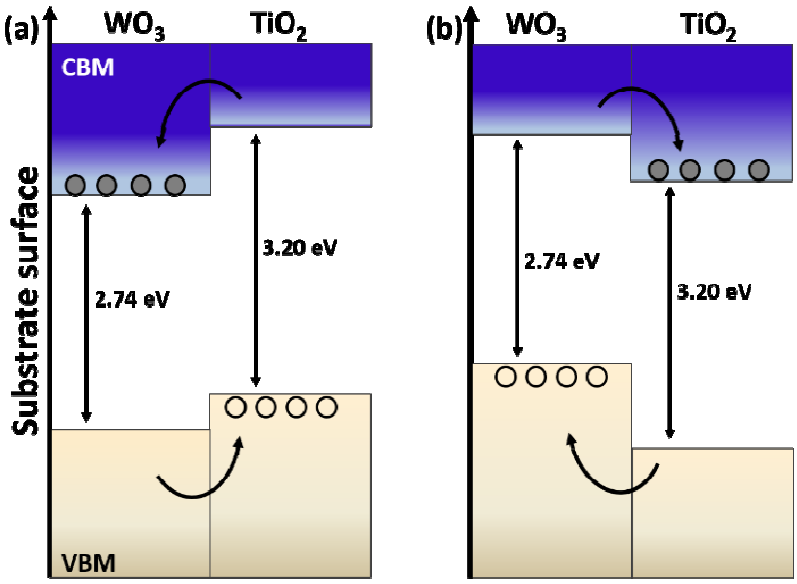

Figure 1. Schematic illustration of two possible band alignments in the WO_3/TiO_2 heterojunction system. Both models are of a staggered type II alignment. In model (A), photogenerated electrons (full circles) transfer from TiO_2 to WO_3 and holes (empty circles) transfer from WO_3 to TiO_2. In the proposed model for our materials (B), a reverse charge transfer is observed.

2. Experimental section

2.1. Synthesis of the WO_3/TiO_2 heterojunction films

Details of the synthesis of the WO_3/TiO_2 heterojunction films as well as reference materials, $WO_3/C/TiO_2$ and P25 *Evonik* films, are given in Supporting Information. Briefly, the WO_3/TiO_2 films were produced following a two-step process using two chemical vapour deposition (CVD) methods. The WO_3 nanorods were deposited using aerosol-assisted CVD from a 2:1 mixture of acetone (99%) and methanol (99.5%) dispersion (15 ml) of tungsten hexacarbonyl ($W(CO)_6$, 0.060 g, 99%). The solution containing the precursors was moistened using an ultrasonic humidifier (*Liquifog*, *Johnson Matthey*) operating at 2 MHz. Pure tungsten trioxide (WO_3) nanorods were deposited as a thin film at a set temperature of 375 ºC (the actual temperature ranged between 339−358 ºC) on quartz slides (*Multi-Lab*). In the optimum WO_3/TiO_2 heterojunction film discussed here the WO_3 nanorods were ~ 650 × 60 nm (length × width). After the synthesis of the WO_3 nanorods, an anatase TiO_2 overlayer was deposited at 500 ºC from titanium tetrachloride ($TiCl_4$, 99%) and ethyl acetate ($C_4H_8O_2$, 99.8 %) using atmospheric-pressure CVD. Each precursor was heated in stainless steel bubblers at 70 and 40 ºC, respectively, and their flow rates set at 1.2 and 0.25 L min^{-1}, respectively. The precursors were mixed in a stainless steel chamber (250 ºC) before accessing the reactor. In the optimum film, the WO_3 nanorods were conformally coated with a TiO_2 overlayer of ~ 100 nm thickness.

2.2. Physical characterisation.

X-ray diffraction (XRD) analysis was performed using a Bruker-Axs D8 (Lynxeye XE) diffractometer. The instrument operates with a Cu X-ray source, monochromated ($K_{\alpha 1}$, 1.54 Å). The films were analysed with a glancing incident angle (θ) of 1 °. Le Bail fits were carried out using structure parameters from Joint Committee on Powder Diffraction Standards (JCPDS), using GSAS and EXPGUI software suit. Raman spectroscopy was carried out using

a Renishaw 1000 spectrometer equipped with a 633 nm laser. The Raman system was calibrated using a silicon reference. UV-Visible spectroscopy was performed using a Perkin Elmer Lambda 950 UV/Vis/NIR Spectrophotometer in the 300−2500 nm range. A *Labsphere* reflectance standard was used as reference in the UV-Visible measurements. Scanning electron microscopy (SEM) studies were carried out using a JEOL 6301 (5 KV) and a JEOL JSM-6700F field emission instruments. High-resolution transmission electron microscopy (HRTEM) images were obtained using a high resolution TEM JEOL 2100 with a LaB_6 source operating at an acceleration voltage of 200 kV. Micrographs were recorded on a Gatan Orius Charge-coupled device (CCD). The films were scrapped off the quartz substrate using a diamond pen, sonicated and suspended in methanol and drop-casted onto a 400 Cu mesh lacy carbon film grid (Agar Scientific Ltd.) for TEM analysis. Energy-dispersive X-ray spectroscopy (EDS) analysis was carried out using a JEOL JSM-6700F and secondary electron image on a Hitachi S-3400N field emission instruments (20 KV) and the Oxford software INCA. Atomic force microscopy (AFM) was conducted using a Bruker Icon system running in PeakForce Quantitative Nanomechanical PropertyMapping (QNM) mode. Bruker NCHV (etched silicon) tips were used in contact mode over a selection of 5 μm × 5 μm areas to measure the topography of the samples. X-ray photoelectron spectroscopy (XPS) was performed using a Thermo K alpha spectrometer with monochromated Al K alpha radiation, a dual beam charge compensation system and constant pass energy of 50 eV. Survey scans were collected in the range of 0−1200 eV. High resolution peaks were used for the principal peaks of Ti (2p), W (4f), O (2p) and C (1s). The peaks were modelled using sensitivity factors to calculate the film composition. The area underneath these bands is an indication of the element concentration within the region of analysis (spot size 400 μm).

2.3. Theoretical characterisation.

All calculations were performed using the Vienna Ab initio Simulation Package (VAS),[17–20] a periodic plane wave density functional theory (DFT) code where the interactions between the core and valence elections are dealt with using the Project Augmented Wave (PAW) method.[21] Both the plane wave basis set and k-point sampling were checked for convergence, with a cutoff of 560 eV and k-point grid of Γ-centred 4 x 4 x 4, for the 32 atom monoclinic unit cell of WO_3 found to be sufficient. Geometry optimisations were performed using the Heyd-Scuseria-Ernzerhof (HSE06) hybrid DFT functional.[22] The structures were deemed to be converged when the forces on all the atoms totalled less than 10 meV $Å^{-1}$. In the plane wave formalism, due to the presence of periodic boundary conditions, the electrostatic potential of a crystal is not defined with respect to an external vacuum level and, as such, the absolute electronic eigenvalues from different calculations are not comparable. In order to align the energies to the vacuum level, a slab-gap model (128 atom, 15.5 Å slab, 20 Å vacuum) was constructed and the corresponding electrostatic potential averaged along the *c*-direction, using the MacroDensity package.[23] Consistent with previous studies of WO_3 surfaces,[24] a $(\sqrt{2} \times \sqrt{2})R45°$ reconstruction of the (001) surface was cleaved using the METADISE code.[25]

2.4. Transient absorption spectroscopy.

Transient absorption spectroscopy, from the microsecond to second timescale, was measured in diffuse reflectance mode. The experimental setup used a Nd:YAG laser (OPOTEK Opolette 355 II, 7 ns pulse width) as the excitation source. 355 nm light was generated from the third harmonic of the laser and transmitted to the sample through a light guide to photoexcite our thin film samples. An excitation power density of 1.2 mJ cm^{-2} and laser repetition rates of 0.9 Hz was used. As the changes of reflectance observed are low (< 1%),

we assume that the transient signal is directly proportional to the concentration of excited state species. The probe light source was a 100 W Bentham IL1 quartz halogen lamp. Long pass filters (*Comar Instruments*) between the lamp and sample were used to minimise short wavelength irradiation of the sample. Diffuse reflectance from the sample was collected by a 2" diameter, 2" focal length lens and relayed to a monochromator (Oriel Cornerstone 130) to select the probe wavelength. Time-resolved intensity data was collected with a Si photodiode (Hamamatsu S3071). Data at times faster than 3.6 ms was recorded by an oscilloscope (Tektronics DPO3012) after passing through an amplifier box (*Costronics*) while data slower than 3.6 ms was simultaneously recorded on a National Instrument DAQ card (NI USB-6251). Each kinetic trace was obtained from the average of 100–200 laser pulses. Acquisitions were triggered by a photodiode (Thorlabs DET10A) exposed to laser scatter. Data was acquired and processed using home-built software written in the Labview environment.

2.5. Photocatalytic tests.

Details of the photocatalytic tests are given in Supplementary Information. A Perkin Elmer RX-I Fourier transform infrared (FTIR) spectrometer was used to monitor the degradation of stearic acid on the films under UVA irradiation. In a typical test, a thin layer of stearic was deposited onto the film using a home-made dip-coater from a 0.05 M stearic acid solution on chloroform. The number of acid molecules degraded was estimated using the conversion factor 1 $cm^{-1} \equiv 9.7 \times 10^{15}$ molecule cm^{-2} from the literature.[26] The photoactivity rates were estimated from linear regression of the initial 30-40 % steps (zero-order kinetics) of the area curves. The results are typically expressed in terms of the formal quantum efficiency, ξ, defined as the number of molecules degraded per incident photon (units, molecules $photon^{-1}$). The light source was a blacklight-bulb lamp (BLB), 2×8 W (*Vilber-Lourmat*). The irradiance of the lamp (I = 3.15 mW cm^{-2}) was measured using a UVX radiometer (UVP).

3. Results.

3.1. Synthesis and physical characterisation.

A range of heterojunction WO_3/TiO_2 thin films were deposited *via* a two-step process using chemical vapour deposition (CVD) methods. A high surface area WO_3 host, which consisted of WO_3 nanorods grown on a quartz substrate, was grown using aerosol-assisted CVD.[27] XPS analysis showed that the WO_3 nanorods synthesised herein are sub-stoichiometric and should be considered as WO_{3-x}, where x = 0.026, XPS results are discussed in depth below. Subsequently these WO_3 nanorods were coated with a conformal TiO_2 layer using atmospheric-pressure CVD.[4] Details of this synthesis procedure are given in the experimental section and Supporting Information. A schematic figure of the TiO_2 coating and corresponding cross-sectional scanning electron microscopy (SEM) images are shown in Figure 2A. The SEM studies confirmed that the microstructure of the WO_3 host was preserved after coating with TiO_2. The average length of the WO_3 rods was estimated as ~ 650 nm, which was found to be ideal from an optical point of view as discussed below. High-resolution transmission electron microscopy (HRTEM) analysis showed that the WO_3 nanorods were completely encapsulated within the TiO_2 overlayer (Figure 2B), forming a core-shell type structure. Complementary energy-dispersive X-ray spectroscopy (EDS) analysis across the nanorods showed a maximum Ti concentration at both edges and the presence of W solely in the core, suggesting no significant W diffusion into the TiO_2 layer. These studies revealed the presence of W, Ti and O only, with no additional impurity elements. EDS showed that the WO_3 nanorods were ~ 60 nm in diameter and that the TiO_2 coating was ~ 100 nm thick.

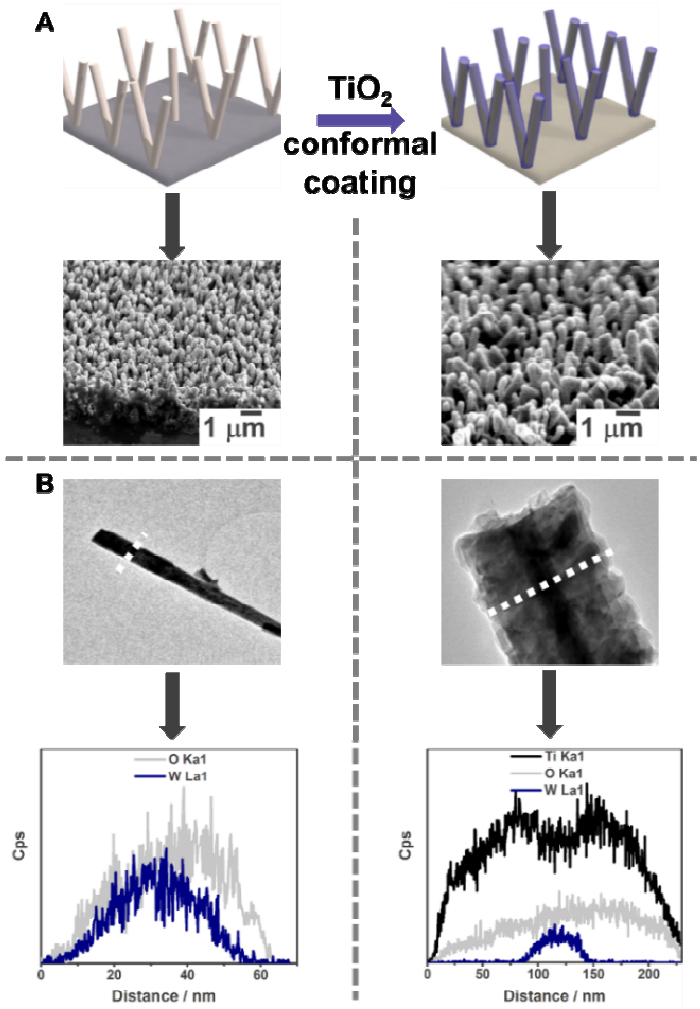

Figure 2. (A) Schematic illustration of the coating of WO_3 nanorods with TiO_2 and their corresponding cross-sectional scanning electron microscopy (SEM) images. (B) High-resolution transmission electron microscopy (HRTEM) images of individual WO_3 nanorods, before (left column) and after (right column) coating with TiO_2 and the corresponding energy dispersive X-ray spectroscopy (EDS) analysis performed across the dotted white line.

X-ray diffraction analysis of the WO_3/TiO_2 heterojunction, and its individual analogues, showed the formation of pure monoclinic WO_3 and anatase TiO_2 structures (Figure 3A) with no trace of additional phases or impurities. Le Bail refined models of the XRD patterns showed no substantial change in unit cell volume for either phase (Table 1), further indicating that no ion diffusion had occurred during the deposition of the TiO_2 overlayer. The corresponding average crystal sizes, determined from diffraction peak widths, did not change significantly from the individual analogues. Raman spectroscopy corroborated our XRD findings, showing the solitary presence of anatase TiO_2 and monoclinic WO_3 phases (Figure

3B). Of note, the position of the main Raman scattering band for anatase (E_g ~ 144 cm^{-1}) is very sensitive to the incorporation of ions within the TiO_2 unit cell.[28] In our WO_3/TiO_2 heterojunctions there was no shift in this band, which again showed that ion diffusion had not occurred.

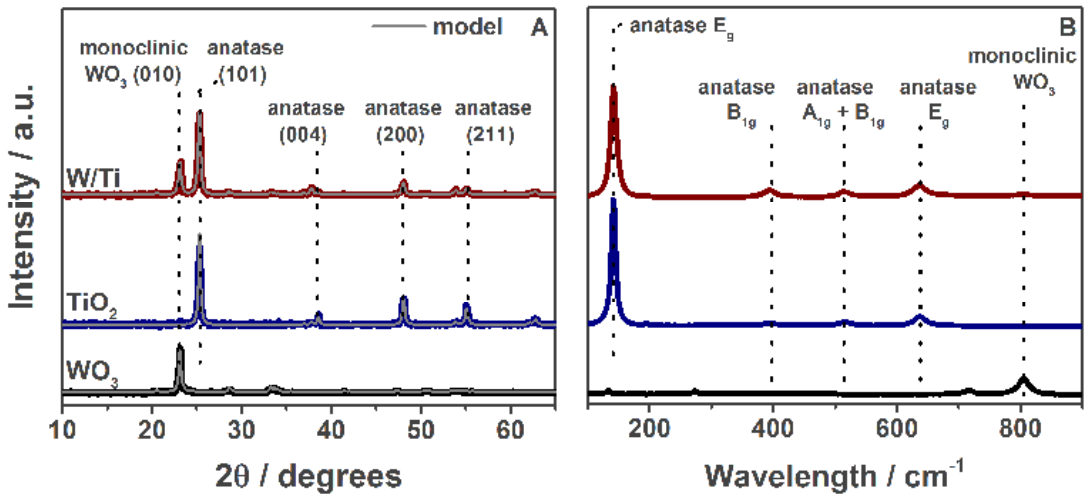

Figure 3. (A) X-ray diffraction patterns of the WO_3/TiO_2 heterojunction film (W/Ti) and its analogues, WO_3 nanorods and anatase TiO_2 (λ = 1.54 Å). The data was fit to a Le Bail refined model (grey lines). (B) Raman spectroscopy analysis showing the presence of pure anatase TiO_2 and monoclinic WO_3 phases. The corresponding XRD peaks and Raman modes of TiO_2 and WO_3 standards (dotted lines) are included for reference.

Table 1. Unit cell lattice parameters derived from Le Bail refinement of XRD data.

Sample		**X-ray diffraction-Le Bail refinement**				
		a [Å]	c [Å]	V (%)	wRp	τ (nm)
Standards	WO_3	7.301(1)	7.670(1)	--	--	--
	TiO_2	3.785(1)	9.512(1)	--	--	--
Pure phase	WO_3	7.287(3)	7.701(1)	0.02	0.12	27.3
Pure phase	TiO_2	3.785(1)	9.525(3)	0.13	0.16	32.6
WO_3/TiO_2	WO_3	7.301(6)	7.710(1)	0.49	0.12	23.2
	TiO_2	3.788(1)	9.515(2)	0.22		26.8

wRp is the weighed residual of least-squares refinement. V (%) is the lattice volume expansion relative to a powder standard. τ is the average crystallite size. Numbers in parentheses represent the error on the last digit.

3.2. Optical properties.

UV-Visible spectroscopy was used to study the optical properties of the WO_3/TiO_2 film and its individual analogues (*i.e.* the WO_3 nanorods before the TiO_2 coating and a conventional TiO_2 film deposited on a plain glass substrate). From Figure 4A, it can be inferred that the single-component TiO_2 film showed the expected absorption edge of the anatase phase at ~ 380 nm. In contrast, the plain WO_3 nanorods showed an absorption edge higher than expected for a WO_3 film, which can be explained in terms of the synthesis method employed. It has been recently found by Ling *et al*.[29] that aerosol-assisted CVD can be used to deposit WO_3 nanorods containing oxygen vacancies, which induce a quantum confinement effect. The existence of oxygen vacancies was inferred from the presence of a small amount of reduced tungsten species ($W^{5+/4+}$) in the as-deposited WO_3 film,[30] as observed by XPS analysis (Figure 4B) and the requirement for charge neutrality. Deconvolution of the W 4f region indicated a relative $W^{5+/4+}$ concentration of *ca*. 2.60 at.%. The formation of dislocation loops within the WO_3 layer would widen the material bandgap, as shown by our Tauc plot analyses,[31] revealing respective bandgaps of *ca*. 3.2 and 3.05 eV for the TiO_2 and WO_3 single-component materials (Figure 4C). However, it is interesting to note that the spectrum of the WO_3/TiO_2 heterojunction was red-shifted to values more akin to bulk WO_3 materials (typically 2.8 eV), with an estimated bandgap of 2.85 eV.

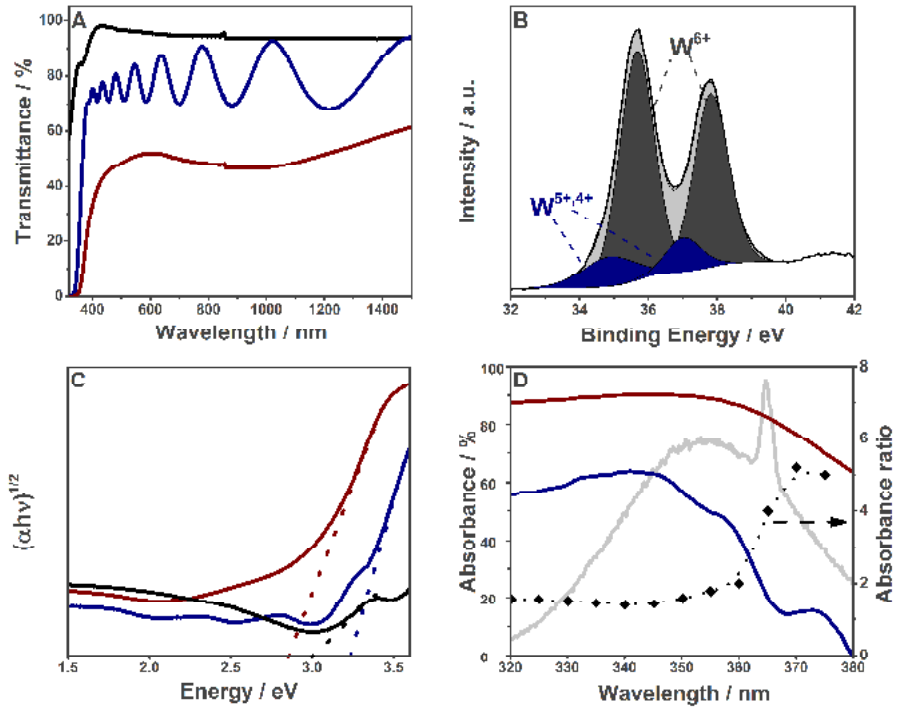

Figure 4. (A) Transmittance spectra of WO_3 (black line), TiO_2 (blue line) and the WO_3/TiO_2 film (red line). (B) X-ray photoelectron spectroscopy (XPS) spectrum of the W 4f environment in films of WO_3. The grey filling is assigned to W^{6+} states and the blue filling is assigned to $W^{5+/4+}$ states. (C) Corresponding bandgap energies derived from Tauc plot analyses. (D) Absorption spectra of the TiO_2 (blue line) and the WO_3/TiO_2 (red line) films in the UV region. The emission spectrum of the UV light source (grey line) used in our photocatalytic tests is included for reference. The dotted line indicates the ratio between the absorbance of the two films.

3.3. Hybrid density functional theory (DFT) and hard X-ray photoelectron spectroscopy (HAXPES) analyses

Further investigation from both theoretical and experimental standpoints was carried out in order to understand the electronic interaction at the WO_3/TiO_2 heterojunction. Density functional theory (DFT) has been widely used to ascertain the electronic band alignment between semiconductors.[32,33] The ionization potential of bulk WO_3 was calculated using the slab model,[23] using hybrid density functional theory (DFT) (HSE06 functional[22]) within the VASP code. In Figure 5, the alignment is plotted relative to the anatase TiO_2 band edges as calculated previously.[3] The HSE06 calculated ionisation potential (7.65 eV) and electron affinity (4.91 eV) for WO_3 fits reasonably well with previous experimental measurements of

7.38 ± 0.11 and 4.10 ± 0.11 eV for WO_3 surfaces.[34] It should be noted that our calculated ionisation potentials do not take into account the effects of interfacial strain and chemical interactions that may influence the band offset at a particular interface, however, they offer a reasonable first approximation, as demonstrated by the widespread application of Anderson's rule for estimating band offsets.[35] Our calculated alignment suggests spatial separation of holes moving into WO_3 (Figure 5). This idealised alignment is at variance with the commonly accepted WO_3–TiO_2 alignment motif in the literature.[12]

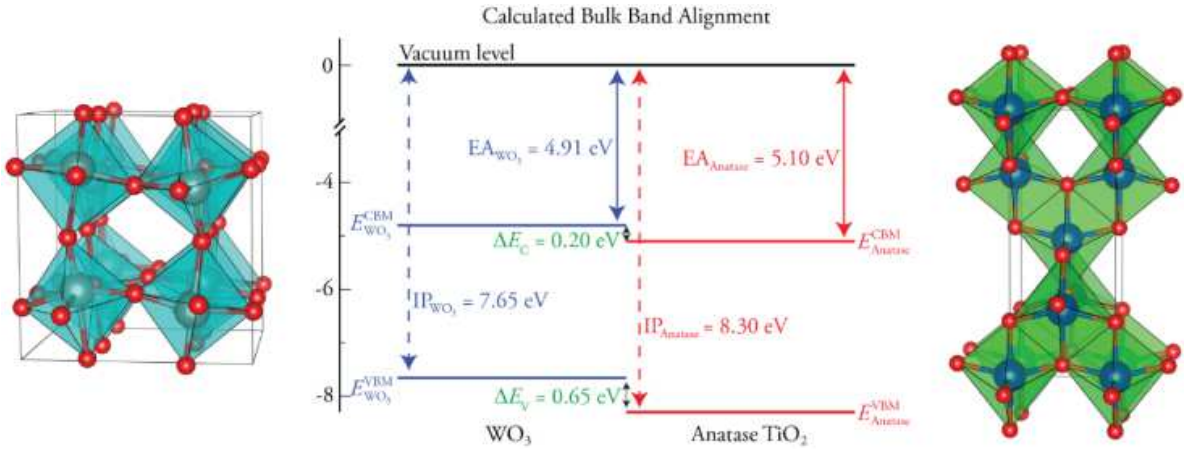

Figure 5. HSE06 calculated band alignment between monoclinic WO_3 and anatase TiO_2. The electron affinities are calculated based on bandgaps of 2.74 and 3.20 eV for WO_3 and TiO_2, respectively.

Further understanding of the electronic processes at the WO_3/TiO_2 interface was revealed from hard X-ray photoelectron spectroscopy (HAXPES) measurements carried out at Beamline I09 at Diamond Light Source. Figure 6A shows the valence band spectra measured from the WO_3/TiO_2 heterojunction film and its individual components. It is worth mentioning that no differences in the binding energy of either Ti 2p or W 4d were detected between the coated nanorods and the corresponding references (see supporting information, Figure S2A and S2B), indicating that the contact between WO_3 and TiO_2 does not alter the energy levels relative to the vacuum level on either side of the interface. A small band observed at ~ 0.5 eV in the WO_3 layer is due to the presence of a small number of W^{5+} defects, typical of WO_3.

The valence band alignment across the WO_3/TiO_2 interface could thus be determined directly from the valence band maxima of the WO_3 and TiO_2 references, which were extracted from Figure 6A to be 2.85 and 3.57 eV below the Fermi level, respectively, leading to a valence band offset of 0.72 eV. Figure 6B summarises the alignment of the energy levels derived from the HAXPES data, where the conduction band offset was estimated to be 0.26 eV, using previously reported bandgaps of 2.74 and 3.2 eV for WO_3 and TiO_2, respectively. It can be seen that the band edge of WO_3 is above that of TiO_2 for both conduction and valence bands, in excellent agreement with our DFT calculations.

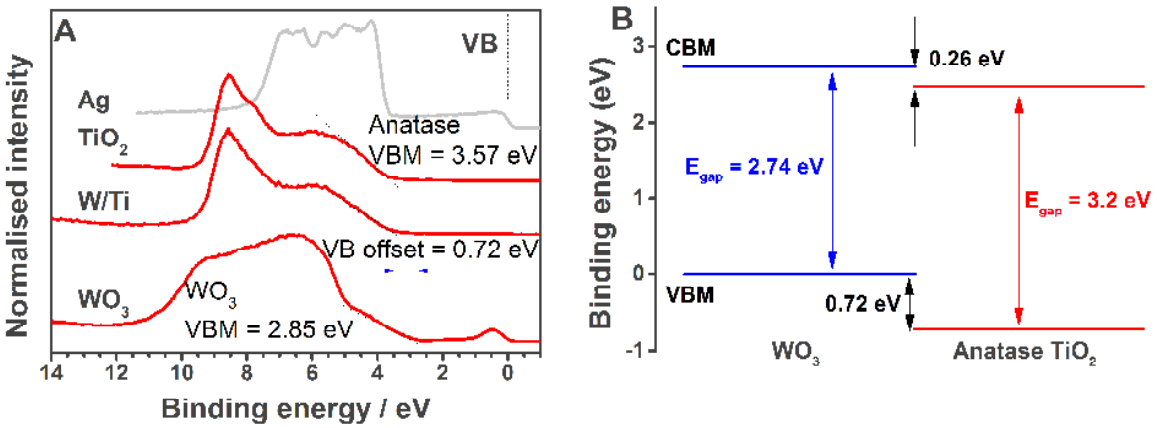

Figure 6. HAXPES measurements of the WO_3/TiO_2 heterojunction film and the individual components, monoclinic WO_3 and anatase TiO_2 films. (A) Corresponding valence band spectra of the three materials. For each sample a silver Fermi edge was recorded to calibrate the binding energies. The blue dashed lines mark the valence band maxima of the TiO_2 and WO_3 references. (B) Band alignment at the WO_3/TiO_2 interface derived from HAXPES results. The conduction band offset was estimated from bandgap energies reported in the literature. The values given are relative to the VBM of WO_3.

3.4. Transient absorption spectroscopy

Transient absorption spectroscopy (TAS) is a form of laser flash spectroscopy that can monitor the generation, recombination, trapping, charge transfer, *etc.* of photogenerated charges in semiconductors.[36–38] The dynamics specific to photogenerated electrons or holes can be studied by tracking transient changes in absorbance at particular wavelengths.[39] The technique has primarily been used to study charge transfer processes in solar cells (organic-

organic or inorganic-organic)[40,41] but has also been used to study charge transfers in heterojunction photocatalysts (inorganic-inorganic)[42] as well as the kinetics of photocatalytic processes.[43,44] In this article, our TAS measurements focused on long lived charge carriers (micro- to millisecond) whose yields and lifetimes are critical to photocatalytic function.[45] The study was carried out in diffuse reflectance mode, since the materials were highly light scattering. A comparison between the TAS measurements of our WO_3/TiO_2 heterojunction film and its individual analogues is shown in Figure 7A. It can be seen that 10 μs after the excitation pulse (λ = 355 nm, 1.2 mJ cm^{-2}), the absorption increase was approximately four times greater than TiO_2. It is worth noting that the pure TiO_2 sample investigated here was 200 nm thick and thus of similar thickness to the TiO_2 overlayer present in our WO_3/TiO_2 heterojunctions.

Chemical scavenger studies of both WO_3 and TiO_2 have shown that photogenerated hole carriers mostly absorb in the near-UV region (λ_{max} ~ 450 nm) and electrons in the near-IR (λ_{max} ~ 900 nm).[10,37] These chemical scavengers are typically required in the case of WO_3 in order to observe charge carriers on the micro-second timescale.[37] This explains the low signals found in WO_3 (Figure 7A), since the measurements were conducted in the absence of chemical scavengers. Transient absorption signals were lost as electrons and holes recombined. This occurred before the timescale of our measurements in WO_3, and substantially more slowly in TiO_2 and WO_3/TiO_2 heterojunction films. The kinetics of electron-hole recombination in our single-component TiO_2 was similar to previous studies.[45,46] If we focus on changes in the transient absorption at 950 nm, which corresponds to photogenerated electrons,[10,37] the rate of recombination is significantly slower within the WO_3/TiO_2 heterojunction compared with TiO_2 (Figure 7B). Because of the strong overlap of charge carriers in WO_3 and TiO_2, our TAS studies could not reveal where the charges

migrated in the heterojunction. However, our results do show that in forming a WO_3/TiO_2 heterojunction both the number of long-lived charge carriers and their lifetime are enhanced.

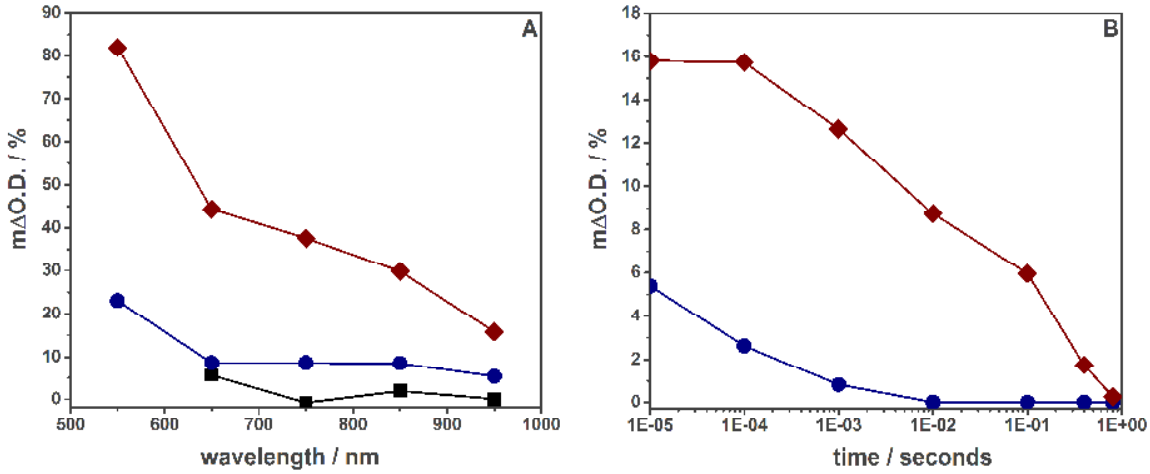

Figure 7. Transient absorption spectroscopy of the WO_3/TiO_2 heterojunction (red line) and its individual components, WO_3 (black line) and TiO_2 (blue line). (A) Transient change in absorption 10 μs after a laser pulse (355 nm, 6 ns pulse width, 1.2 mJ cm^{-2} $pulse^{-1}$). (B) Decay in transient absorption at 950 nm, which represents the recombination of photogenerated electrons located in either the WO_3 or TiO_2 layers.

3.5. Photocatalytic activity

The photocatalytic activities of the WO_3/TiO_2 film and their analogues were evaluated against the degradation of a model organic pollutant, octadecanoic (stearic) acid, under ultraviolet (UVA) illumination (I = 3.15 mW cm^{-2}).[26] Details of the photocatalytic test are given in the experimental section and Supplementary Information. The rates of degradation were conveniently expressed in terms of formal quantum efficiency (ξ, units, molecules $photon^{-1}$), defined as molecules of stearic acid degraded per incident photon. The corresponding values are listed in Table 2. The photocatalytic activity of the heterojunction film (17.1×10^{-4} molecules $photon^{-1}$) was clearly superior to those of the WO_3 and TiO_2 individual analogues (0.4×10^{-4} and 1.3×10^{-4} molecules $photon^{-1}$, respectively). If we consider the number of electron transfers required to completely photocatalyse stearic acid (104 electrons),[47] then a formal quantum efficiency of 17.1×10^{-4} molecules $photon^{-1}$ corresponds to a photocatalytic efficiency of ~ 18 % per incident photon. Figure 8 compares these ξ values with those

obtained using standard samples. Remarkably, the activity of the WO_3/TiO_2 thin film was comparable to that of a thick TiO_2 P25 *Evonik* film (16.8×10^{-4} molecules photon^{-1}) prepared following a method from the literature (see Supporting Information).[48] As a reference, this study included a commercially available self-cleaning coating, Pilkington Activ^{TM} glass obtained from Mills *et al*.[49] (Figure 8), which showed a ξ value of 0.2×10^{-4} molecules photon^{-1}. It is worth noting that the activity of the WO_3/TiO_2 film exceeded that of a highly active heterojunction rutile/anatase TiO_2 film (10.7×10^{-4} molecules photon^{-1}) previously synthesised in our group (Table 2 and Figure 8).[4] The ξ values were also highly reproducible, even after storage for one year (Figure S3).

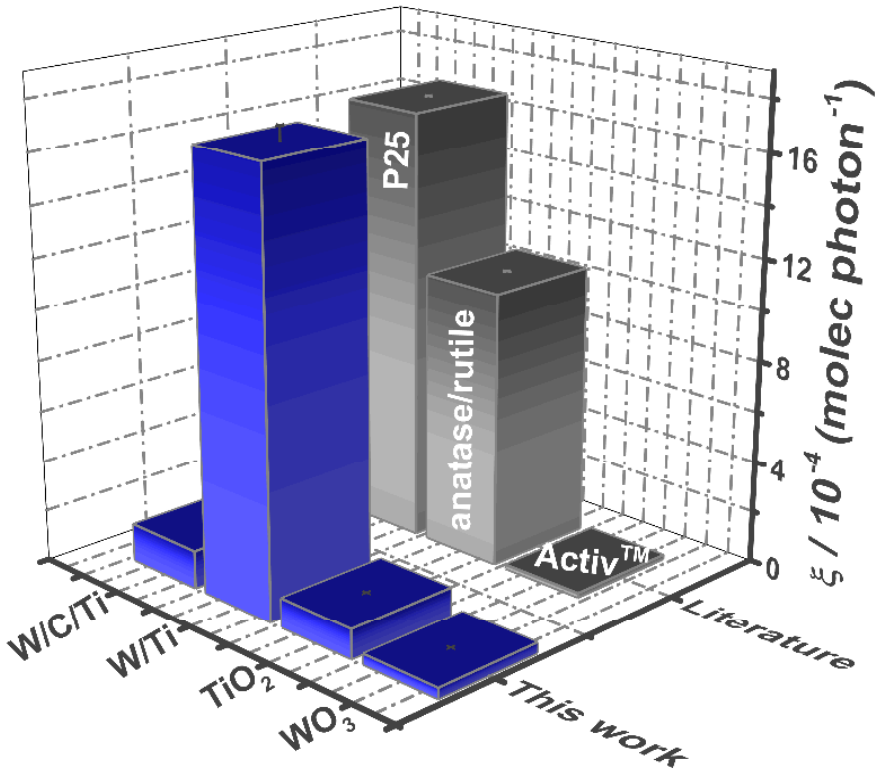

Figure 8. Photocatalytic activities of the WO_3/TiO_2 heterojunction (W/Ti), its individual analogues WO_3 and TiO_2, and a $WO_3/C/TiO_2$ (W/C/Ti) film, where a carbon layer was deposited between the WO_3 and TiO_2 layers. These results are expressed as formal quantum efficiencies (ξ), which represent the rate of stearic acid molecules degraded per incident photon (molecule photon^{-1}) under UVA illumination ($I = 3.15$ mW·cm^{-2}). Typical ξ values of relevant photocatalytic materials are included for reference. The corresponding activities of Pilkington Activ^{TM} and the rutile/anatase heterojunction TiO_2 films were obtained from references [**49** and **4**].

Table 2. Relevant physical and functional details of the WO_3/TiO_2 film, individual analogues and reference samples.

Sample	Physical Properties			Functional properties
	Microscopy			Photocatalysis
	d (nm)	E_{bg} (eV)	Surface Area (μm^2)	ξ / 10^{-4} (molecules photon^{-1})
WO_3	--	3.10	11.1(3)	0.4 ± 0.06
TiO_2[a]	650	3.21	4.6(4)	1.3 ± 0.04
WO_3/TiO_2	100	2.85	7.6(7)	17.1 ± 0.35
$WO_3/C/TiO_2$	100	--	7.2(7)	1.5 ± 0.07
P25 *Evonik*	1300	--	--	16.8 ± 0.03

[a]Values for a single-component TiO_2 thin film deposited on a quartz substrate under identical flow/temperature conditions and deposition time as the WO_3/TiO_2 heterojunction film. Film thickness (d) was of the TiO_2 layer alone and estimated using TEM, SEM and profilometry measurements. Bandgap energy values (E_{bg}) were estimated from Tauc plot analysis.

4. Discussion

Many research groups have investigated the interaction between WO_3 and TiO_2 using different synthesis methods.[12–14,50–52] Commonly, these resulted in triclinic WO_3 as opposed to the monoclinic structure formed in this work, which also showed a strong preferred orientation in the [002] crystal plane. The apparent inversion of the charge carrier transfer observed in our case, with electrons moving from WO_3 to TiO_2, could indeed be associated with structural differences, resulting in different electronic properties that alter the interaction between the two semiconductors. For instance, Kafizas *et* al.[10] found that hole transfer in the anatase/ rutile TiO_2 heterojunction flowed in a reverse direction to band model predictions determined by both computation and experiment,[3] which was attributed to the presence of intra-bandgap defect energy levels at the heterojunction interface. Many works reported in the literature use WO_3/TiO_2 composites rather than clearly defined heterojunctions.[14,51,53] Makwana *et al*.[16] developed cold-pressed WO_3/TiO_2 pellets, and found that the colour of the

WO_3 layer changed from yellow to blue upon radiation, resulting in the formation of reduced $W^{5+/4+}$ species. However, our computational and HAXPES studies showed complementary evidence for a monoclinic WO_3/ anatase TiO_2 band alignment that favours the transfer of photogenerated electrons into TiO_2 and holes into WO_3 (Figures 5 and 6). This direction of electron transfer is supported by the fact that no colour change was observed in our WO_3/TiO_2 heterojunction films, even after long periods of intense ultraviolet illumination (*i.e.* several days at ~ 3 $mW.cm^{-2}$).

It is worth noting that, despite the different synthetic routes and crystal structures, the WO_3/TiO_2 heterojunction system has typically shown an enhancement in function compared to the individual analogues. It is also important to establish whether the enhanced activity of the WO_3/TiO_2 film correlates with a favourable light absorption compared to its individual components. The conventional evaluation of photocatalytic activity using formal quantum efficiencies (ξ) assumes that all incident photons are effectively absorbed by the films. Ideally, the activity should be expressed in terms of quantum yield, which considers the number of absorbed photons in this evaluation. Unfortunately, this estimation is not always straightforward, particularly when using light sources of relatively broad emission spectra. As previously mentioned, the absorption spectrum of the heterojunction film showed a band onset that was substantially red-shifted compared to those of each isolated analogue. Figure 4D highlights the absorption of this film compared to a pure TiO_2 film. As indicated in the figure, it can be clearly observed that the absorption of the heterojunction film was approximately 4 times higher than that of the TiO_2 film at the maximum emission wavelength of the lamp (λ_{max} = 365 nm). While this is an important advantage for the WO_3/TiO_2 film, the enhancement in activity observed (14-fold with respect to TiO_2) cannot be explained solely in terms of light absorption.

The efficiency of a system in heterogeneous photocatalysis is also strongly related to the specific surface area of the catalyst. Considering the surface roughness of our WO_3/TiO_2 film, it was important to evaluate whether the enhanced photocatalytic activity of this film could be merely attributed to an increased in surface area rather than to any electronic advantage at the heterojunction level.[5] Hence, an experiment was designed where a thin layer of carbon was sputtered over the WO_3 nanorods before the deposition of the TiO_2 layer in order to inhibit direct contact between the oxide phases. As observed by SEM (Figure S1), the resulting $WO_3/C/TiO_2$ film had a similar microstructure than that of the WO_3/TiO_2 film. Despite the similar morphology, the $WO_3/C/TiO_2$ film only showed a slight increase in photocatalytic activity over the pure TiO_2 film (Figure 8) and thus the enhanced activity of the WO_3/TiO_2 film was attributed mainly to a synergistic interaction between the two semiconductors.

As previously shown, this synergistic interaction was unequivocally confirmed by our TAS studies, which showed an enhanced charge carrier population and lifetime of photogenerated charge (Figure 7). In terms of the lack of function observed in $WO_3/C/TiO_2$ our triple-junction, we attribute this to unfavourable band-bending at both semiconductor-metal interfaces, which forms and ohmic contact that encourages the flow of photogenerated electrons into the carbon layer (full details of our band modelling are provided in the Supplementary Information, Figure S4).

It is widely accepted that most photocatalytic processes on TiO_2, when conducted at ambient conditions, proceed *via* the generation of hydroxyl and superoxide radicals (from the reaction of photogenerated charges with surface-bound water and di-oxygen species, respectively) that are highly active in the decomposition of organic species.[54] The timescales in which these processes occur have been studied using TAS, being in the microsecond and millisecond timescales for the respective formation of hydroxyl radicals and superoxide species.[55,56] Our TAS studies showed that there was a ~ 20-fold increase in the number of photogenerated

electrons in our WO_3/TiO_2 heterojunction compared with TiO_2 from the millisecond timescale – the timescale relevant to the formation of superoxide. In addition, the rate at which these charges recombined was substantially slowed, likely reducing the competition between recombination and photogeneration. An interesting question remains as to the role of photogenerated holes in our WO_3/TiO_2 heterojunction structure. We therefore speculate that these holes either remain within the WO_3 layer and drive the formation of hydroxyl radicals at breaks in the TiO_2 coating or, more likely, also migrate into the TiO_2 layer through intra-bandgap trap-states.

It is worth comparing the photocatalytic efficiency of our WO_3/TiO_2 heterojunction with the enhancements observed for different heterojunction systems and chemically modified photocatalysts. Unfortunately, a direct comparison of the photocatalytic activity with previous studies of WO_3/TiO_2 could not be conducted, as these studies were mainly based on changes in hydrophilicity.[12,52] There is also an inherent difficulty to compare photocatalytic materials produced by different synthetic methods and research groups. This issue was bypassed herein by comparing *enhancement factors* of materials synthesised in our group using the same photocatalytic test, the degradation of stearic acid (Table 3). This *enhancement factor* was estimated from activity ratios between the heterojunction (or doped) material and their corresponding best-performing single (or pure) component. For instance, the enhancement factor for the system reported by Quesada-Cabrera *et al*.,[4] rutile/anatase TiO_2 heterojunction, was calculated by taking the ξ value for the heterojunction system and the most active single-component, anatase TiO_2, these values being ~ 7.0 and ~ 0.74 molecules photon^{-1}, respectively, and thus the estimated enhancement factor is ~ 8. As observed in Table 3, the corresponding enhancement factor of our WO_3/TiO_2 system is ~ 14, which is the highest enhancement ever reported, to the best of our knowledge. A more comprehensive comparison with the literature is shown in the Supporting Information (Table S1).

Table 3. Photocatalytic enhancement factors of representative heterojunction and doped materials reported in the literature. Synthetic method and photocatalytic test are included as reference. All photocatalytic materials were compared to their individual analogues.

Photocatalyst	Synthesis method	Test	λ	Enhancement factor[a]	Refs.
WO_3/TiO_2	(AP)CVD	Stearic acid	UVA	14	**This work**
Rutile/Anatase TiO_2	(AP)CVD	Stearic acid	UVA	8	**4**
Nano-Au:Ag:TiO_2	Sol-gel	Stearic acid	UVA	7	**57**
W:TiO_2	Sol-gel	Stearic acid	UVA	5	**57**
N:TiO_2	(AP)CVD	Stearic acid	UVA	3.5	**58**

[a]Approximate enhancement factors estimated from activity ratios between the heterojunction (or chemically-modified/doped) material and the corresponding active analogue (or pure) component.

5. Conclusion

Nanostructured WO_3/TiO_2 heterojunction films were grown using chemical vapour deposition. To the best of our knowledge, the optimised WO_3/TiO_2 film showed the highest enhancement in photocatalytic activity compared to its single-semiconductor analogues. The WO_3/TiO_2 heterojunctions showed an unusual electron transfer from WO_3 to TiO_2. A direct understanding of this charge transfer process was provided through both computational calculation and experiment (HAXPES and TAS).

Importantly, the WO_3/TiO_2 films are durable and the results observed are highly reproducible over multiple photocatalytic cycles. The methods described here represent a breakthrough in the development of photocatalytic surfaces and highlight the advantage of using a combination of key experimental and computational techniques to develop our understanding of photocatalytic heterojunction materials, and should serve as guide to future advances in the field.

Supporting Information

The Supporting Information shows in detail the synthesis of the WO_3/TiO_2 heterojunction, single-semiconductor analogues (WO_3 and TiO_2), as well two the two control samples used in this work ($WO_3/C/TiO_2$ heterojunction system and P25 *Evonik* film). Scanning electron microscopy images (SEM) of WO_3 nanorods, WO_3/TiO_2 and $WO_3/C/TiO_2$ heterojunction films, as well as atomic force microscopy (AFM) images of the WO_3/TiO_2, are shown in Figure S1. Hard X-ray photoelectron spectroscopy spectra of the binding energy of either Ti 2p or W 4d peaks are shown in Figure S2. Photocatalytic degradation of stearic acid under UVA light, infrared spectra, integrated areas and sequential photocatalytic tests are shown in Figure S3. Band bending details of the $WO_3/C/TiO_2$ heterojunction film are shown in Figure S4. Supporting Information is available from the Wiley Online Library or from the author.

Acknowledgements

CSV and RQC were supported by the European Seventh Framework Programme (PCATDES project, N. 309846). This work made use of the ARCHER UK National Supercomputing Service (http://www.archer.ac.uk), via our membership of the UK's HEC Materials Chemistry Consortium, which is funded by EPSRC (EP/L000202). AK thanks the Ramsay Memorial Fellowships Trust for funding. Dr. Sanjay Sathasivam and Mr. Francesco Di Maggio are thanked for useful discussion. Dr. Steven Firth and Mr. Martin Vickers are also thanked for access to SEM, TEM, Raman and XRD instruments.

Received: ((will be filled in by the editorial staff))
Revised: ((will be filled in by the editorial staff))
Published online: ((will be filled in by the editorial staff))

References

(1) Gratzel, M. *J. Photochem. Photobio. C*. **2003**, *4*, 145.

(2) Moniz, S. J. A.; Shevlin, S. A.; Martin, D. J.; Guo, Z.-X.; Tang, J. *Energy Environ. Sci.* **2015**, *8*, 715.

(3) Scanlon, D. O.; Dunnill, C. W.; Buckeridge, J.; Shevlin, S. A; Logsdail, A. J.; Woodley, S. M.; Catlow, C. R. A; Powell, M. J.; Palgrave, R. G.; Parkin, I. P.; Watson, G. W.; Keal, T. W.; Sherwood, P.; Walsh, A.; Sokol, A. A. *Nat. Mater.* **2013**, *12* (9), 798.

(4) Quesada-Cabrera, R.; Sotelo-Vazquez, C.; Bear, J. C.; Darr, J. A.; Parkin, I. P. *Adv. Mater. Interfaces*. **2014**, *1*, 1400069.

(5) Wang, H.; Zhang, L.; Chen, Z.; Hu, J.; Li, S. *Chem. Soc. Rev*. **2014**, *43*, 5234.

(6) Ohtani, B.; Prieto-Mahaney, O. O.; Li, D.; Abe, R. *J. Photochem. Photobiol. A Chem.* **2010**, *216*, 179.

(7) Paracchino, A.; Laporte, V.; Sivula, K.; Gratzel, M; Thimsen, E. *Nat. Mater.* **2011**, *10*

(6), 456.

(8) Su, J.; Guo, L.; Bao, N.; Grimes, C. A. *Nano Lett*. **2011**, 1928.

(9) Moniz, S. J. A.; Zhu, J.; Tang, J. *Adv. Energy Mater*. **2014**, *4*, 1301590.

(10) Kafizas, A.; Wang, X.; Pendlebury, S. R.; Barnes, P.; Ling, M.; Sotelo-Vazquez, C.; Quesada-Cabrera, R.; Li, C.; Parkin, I. P.; Durrant, J. R. *J. Phys. Chem. A*. **2016**, *120*, 715.

(11) Hurum, D. C.; Agrios, A. G.; Gray, K. A.; Rajh, T.; Thurnauer, M. C. *J. Phys. Chem. B*. **2003**, *107*, 4545.

(12) Miyauchi, M.; Nakajima, A.; Watanabe, T.; Hashimoto, K. *Chem. Mater*. **2002**, *14*, 4714.

(13) Smith, W.; Wolcott, A.; Fitzmorris, R. C.; Zhang, J. Z.; Zhao, Y. *J Mater Chem*. **2011**, *21*, 10792.

(14) Higashimoto, S.; Sakiyama, M.; Azuma, M. *Thin Solid Film*. **2006**, *503*, 201.

(15) Leftheriotis, G.; Papaefthimiou, S.; Yianoulis, P.; Siokou, A. *Thin Solid Film*. **2001**, *384*, 298.

(16) Makwana, N. M.; Quesada-cabrera, R.; Parkin, I. P.; Mcmillan, P. F.; Mills, A.; Darr, J. A. *J. Mater. Chem. A Mater.* **2014**, *2*, 17602.

(17) Kresse, G. & Hafner, J. *Phys. Rev. B. PRB*. **1993**, *47*, 558

(18) Kresse, G. & Hafner, J. *Phys. Rev. B, PRB*. **1994**, *49***,** 14251.

(19) Kresse, G.; Furthmuller, J. *Phys. Rev. B, PRB*. **1996**, *54*, 11169.

(20) Kresse, G.; Furthmuller, J. *Comput. Mater. Sci.* **1996**, *6*, 15.

(21) Kresse, G.; Joubert, D. *Phys. Rev. B, PRB*. **1999**, *59* (3), 11.

(22) Krukau, A. V; Vydrov, O. A.; Izmaylov, A. F.; Scuseria, G. E. *J. Chem. Phys*. **2007**, *1225*, 224106.

(23) Burton, L. A.; Walsh, A. *Appl. Phys. Lett*. **2016**, *120*, 132111.

(24) Oliver, P. M.; Parker, S. C.; Egdell, R. G.; Jones, F. H. *J. Chem. Soc., Faraday Trans.*

1996, *92* (12), 2049.

(25) Watson, G. W.; Kelsey, E. T.; Leeuw, N. H. De; Harris, D. J.; Parker, S. C. *J. Chem. Soc., Faraday Trans.* **1996**, *92* (3), 433.

(26) Mills, A.; Wang, J. *J. Photochem. Photobiol. A Chem.* **2006**, *182* (2), 181.

(27) Ling, M.; Blackman, C. *Phys. Status Solidi C*. **2015**, *12*, 869.

(28) Kafizas, A.; Parkin, I. P. *J. Am. Chem. Soc.* **2011**, *133* (50), 20458.

(29) Ling, M.; Blackman, C.; Palgrave, R.; Kafizas, A. *Nanoscale.* **2016**, NR-ART-08-2016-006689.

(30) Smith, A. M.; Kast, M. G.; Nail, B. A.; Aloni, S.; Boettcher, S. W. *J. Mater. Chem. A*. **2014**, *2*, 6121.

(31) Tauc, J. *Mater. Res. Bull.* **1968**, *3* (1), 37.

(32) Hinuma, Y.; Gruneis, A.; Kresse, G.; Oba, F. *Phys. Rev. B*. **2014**, *90*, 155405.

(33) Buckeridge, J.; Butler, K. T.; Catlow, C. R. A.; Logsdail, A. J.; Scanlon, D. O.; Shevlin, S. A.; Woodley, S. M.; Sokol, A. A.; Walsh, A. *Chem. Mater*. **2015**, *27*, 132111.

(34) Weinhardt, L.; Blum, M.; Bar, M.; Heske, C.; Cole, B.; Marsen, B.; Miller, E. L. *J. Phys. Chem. C*. **2008**, *112*, 3078.

(35) Anderson, R. L. *IBM J. Res. Dev*. **1960**, *4*, 283.

(36) Pendlebury, S. R.; Wang, X.; Formal, F. Le; Cornuz, M.; Kafizas, A.; Tilley, S. D.; Gra, M.; Durrant, J. R. *J. Am. Chem. Soc*. **2014**, *163*, 9854.

(37) Pesci, F. M.; Cowan, A. J.; Alexander, B. D.; Durrant, J. R.; Klug, D. R. *J. Phys. Chem. Lett.* **2011**, *2*, 1900.

(38) Ma, Y.; Pendlebury, S. R.; Reynal, A.; Formal, F. Le; Durrant, J. R. *Chem. Sci*. **2014**, *5*, 2964.

(39) Fujishima, A.; Zhang, X.; Tryk, D. *Surf. Sci. Rep.* **2008**, *63* (12), 515.

(40) Wang, L.; Mccleese, C.; Kovalsky, A.; Zhao, Y.; Burda, C. *J. Am. Chem. Soc*. **2014**, *163*, 12205.

(41) Clarke, T. M.; Jamieson, F. C.; Durrant, J. R. *J. Phys. Chem. C*. **2009**, *113*, 20934.

(42) Wang, L.; Wang, H.-Y.; Gao, B.-R.; Pan, L.-Y.; Jiang, Y.; Chen, Q.-D.; Han, W.; Sun, H.-B. *IEEE J. Quantum Electron.* **2011**, *47* (9), 1177.

(43) Devahasdin, S.; Fan, C.; Li, K.; Chen, D. H. *J. Photochem. Photobiol. A Chem.* **2003**, *156* (1-3), 161.

(44) Tang, J.; Durrant, J. R.; Klug, D. R. *J. Am. Chem. Soc.* **2008**, *130* (42), 13885.

(45) Wang, X.; Ka, A.; Li, X.; Moniz, S. J. A.; Reardon, P. J. T.; Tang, J.; Parkin, I. P.; Durrant, J. R. *J. Phys. Chem. C*. **2015**, *119*, 10439.

(46) Cowan, A. J.; Leng, W.; Barnes, P. R. F.; Klug, D. R; Durrant, J. R. *Phys. Chem. Chem. Phys*. **2013**, *15*, 8772.

(47) Mills, A.; McFarlane, M. *Catal. Today* **2007**, *129* (1–2), 22.

(48) Mills, A.; Wang, J. *J. Photochem. Photobiol. A Chem.* **1998**, *118*, 53.

(49) Mills, A.; Lepre, A.; Elliott, N.; Bhopal, S.; Parkin, I. P.; Neill, S. A. O. *J. Photochem. Photobiol. A Chem.* **2003**, *160*, 213.

(50) Lu, B.; Li, X.; Wang, T.; Xie, E.; Xu, Z. *J. Mater. Chem. A*. **2013**, *1*, 3900.

(51) Quesada-Cabrera, R. Q.; Latimer, E. R.; Kafizas, A.; Blackman, C. S.; Carmalt, C. J.; Parkin, I. P. *J. Photochem. Photobiol. A Chem.* **2012**, *239*, 60.

(52) Irie, H.; Mori, H.; Hashimoto, K. *Vacuum*. **2004**, *74*, 625.

(53) Puddu, V.; Mokaya, R.; Puma, G. Li. *Chem. Comm.* **2007**, *45*, 4749.

(54) Mills, A.; Hunte, S. Le. *J. Photochem. Photobiol. A Chem.* **1997**, *108*, 1.

(55) Yamakata, A.; Ishibashi, T.; Onishi, H. *J. Phys. Chem. B*. **2001**, *105*, 7258.

(56) Xiao-e, L.; Green, A. N. M.; Haque, S. A.; Mills, A.; Durrant, J. R. *J. Photochem. Photobiol. A Chem*. **2004**, *162*, 253.

(57) Kafizas, A.; Kellici, S.; Darr, J. A; Parkin, I. P. *J. Photochem. Photobiol. A Chem.* **2009**, *204*, 183.

(58) Sotelo-Vazquez, C.; Quesada-Cabrera, R.; Darr, J. A.; Parkin, I. P. *J. Mater. Chem. A*.

2014, *2*, 7082.

Keyword

Carlos Sotelo-Vazquez[1], Raul Quesada-Cabrera[1]*, Min Ling[1], David O. Scanlon[1,2], Andreas Kafizas[1], Pardeep Kumar Thakur[2], Tien-Lin Lee[2], Alaric Taylor[3], Graeme W. Watson[4], Robert G. Palgrave[1], James R. Durrant[5], Christopher S. Blackman[1], and Ivan P. Parkin[1]*

Evidence and effect of photogenerated charge transfer for enhanced photocatalysis in WO_3/TiO_2 heterojunction films: a computational and experimental study.

ToC figure ((Please choose one size: 55 mm broad × 50 mm high **or** 110 mm broad × 20 mm high. Please do not use any other dimensions))

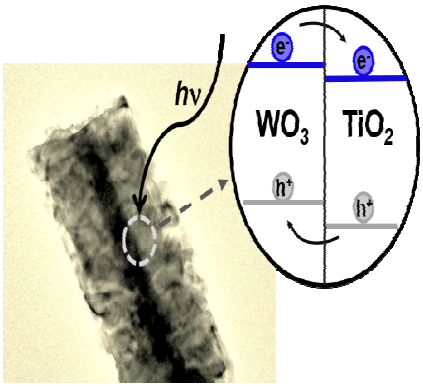

Supporting Information

Evidence and effect of photogenerated charge transfer for enhanced photocatalysis in WO_3/TiO_2 heterojunction films: a computational and experimental study.

Carlos Sotelo-Vazquez[1], Raul Quesada-Cabrera[1], Min Ling[1], David O. Scanlon[1,2], Andreas Kafizas[1], Pardeep Kumar Thakur[2], Tien-Lin Lee[2], Alaric Taylor[3], Graeme W. Watson[4], Robert G. Palgrave[1], James R. Durrant[5], Christopher S. Blackman[1], and Ivan P. Parkin[1]**

1. Synthesis of WO_3/TiO_2 heterojunction films and control samples.

The WO_3/TiO_2 heterojunction films were produced following a two-step process using two chemical vapour deposition (CVD) methods. In the synthesis of the optimised WO_3/TiO_2 heterojunction film, a first layer of WO_3 nanorods (~ 650 × 60 nm, length × width) deposited using aerosol-assisted CVD was conformally coated with a layer of anatase TiO_2 (~ 100 nm thickness) using atmospheric-pressure CVD. These methods only differ in the way the precursors are introduced in the CVD reactor, as explained below. The precursors were carried into the reactor chamber using nitrogen (N_2) as an inert carrier gas (supplied by *BOC*). The gases are introduced through a designed stainless steel baffle manifold in order to ensure a laminar flow in the reactor. All heating elements in the systems were controlled using Pt-Rh thermocouples. All chemicals were purchased from *Sigma-Aldrich* unless stated otherwise.

1.1. Aerosol-assisted chemical vapour deposition (AACVD): WO_3 nanorods.

Tungsten hexacarbonyl (0.060 g) ($W(CO)_6$, 99 %) was dissolved in 15 ml of a 2:1 mixture of acetone (99%, *Emplura*) and methanol (99.5%, *Emplura*). The solution containing the

precursors was moistened using an ultrasonic humidifier (*Liquifog, Johnson Matthey*), operating at 2 MHz, and carried into the CVD reactor by the carrier gas. Pure tungsten trioxide (WO_3) nanorods were deposited as a thin film at a set temperature of 375 °C (the actual temperature ranged between 339−358 °C) on quartz slides (*Multi-Lab*, 25 × 25 × 2 mm, length × width × thickness).[1] The quartz substrates were thoroughly cleaned using acetone (99 %), isopropanol (99.9 %) and distilled water and dried in air prior to use. A typical SEM image of the WO_3 nanorods is shown in Figure S1A.

1.2. Atmospheric-pressure chemical vapor deposition (APCVD): TiO_2 coating.

After the synthesis of WO_3 nanorods, a TiO_2 coating was deposited at 500 °C from titanium tetrachloride ($TiCl_4$, 99 %) and ethyl acetate ($C_4H_8O_2$, 99.8 %) using APCVD. In this case, each precursor ($TiCl_4$ and $C_4H_8O_2$) was heated in stainless steel bubblers at 70 and 40 °C and their flow rates set at 1.2 and 0.25 L min^{-1}, respectively.[2] The APCVD reactor was a cold-wall unit which consisted of a 320 mm-long heating graphite block accommodated in a quartz tube. The graphite block had three inserted *Whatman* heater cartridges. The precursors were carried into the reactor chamber using pre-heated (200 °C) nitrogen (N_2) as an inert carrier gas (supplied by *BOC*) In APCVD, the precursors are mixed in a stainless steel chamber (250 ºC) before accessing the reactor. The entire CVD rig is kept at high temperature (>200 ºC) using pipe heaters.

Under these synthesis conditions, the deposition time was strictly controlled during synthesis of the TiO_2 layer (60 s) in order to achieve a conformal coating of the WO_3 nanorods. As observed in Figure S1B, the deposition of the TiO_2 overlayer did not alter the original microstructure of the WO_3 nanorods.

1.3. Synthesis of control sample: WO_3/C/TiO_2 film.

The conditions described above for the WO_3/TiO_2 heterojunction film were reproduced with the incorporation of a thin carbon interlayer, which was sputtered over the WO_3 nanorods before the deposition of the TiO_2 layer. This carbon interlayer inhibited direct contact between WO_3 and TiO_2 phases whilst preserving the microstructure of the original WO_3/TiO_2 film (Figure S1C). This was important in order to ascertain whether the enhancement in activity observed when comparing the nanostructured WO_3/TiO_2 and the *flat* TiO_2 reference was simply due to an increased specific surface area. Atomic force microscopy (AFM) measurements of the WO_3 nanorods, WO_3/TiO_2 (Figure S1D) and WO_3/C/TiO_2 films showed surface area values of a similar order (Table 2 main text).

1.4. Synthesis of control sample: P25 Evonik film.

A commercial P25 *Evonik* TiO_2 film was deposited on a borosilicate glass slide (75 × 25 × 1 mm, *VWR International*) by dip-coating into a 5 wt% aqueous dispersion, following the optimum conditions reported by Mills *et al*.[3] In the current work the glass slide was immersed in the dispersion for 10 s and then withdrawn at 120 mm min^{-1}. The film was dried at 30 °C for 30 min and then at 100 °C for 1 h, before washing it with water and left it to dry in air. This process was repeated 3 times. The average thickness of the film was 1.3 ± 0.2 μm, as estimated from profilometry measurements. The TiO_2 coating on the back of the substrate was removed using a NaOH 5 M solution.

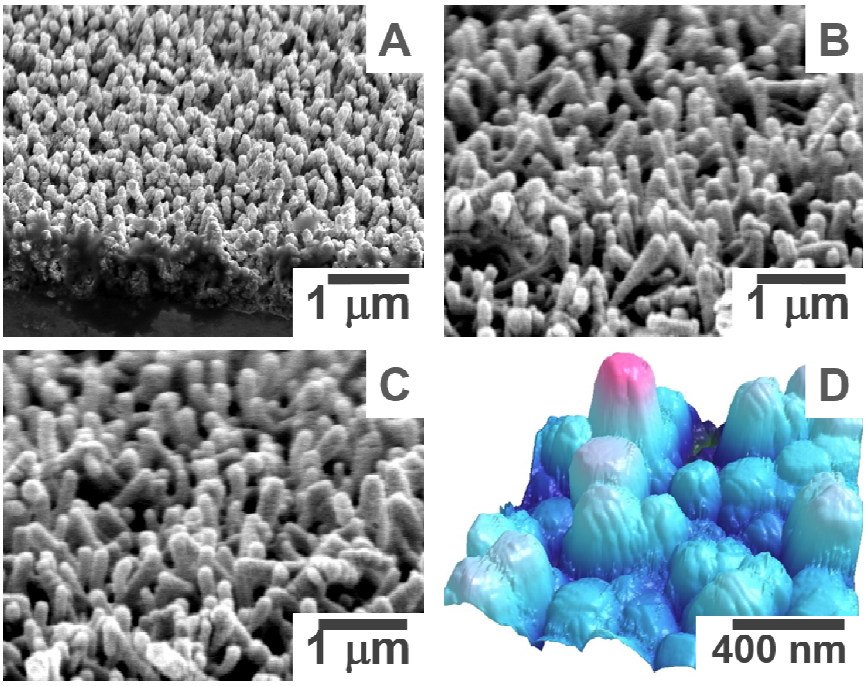

Figure S1. Scanning electron microscopy (SEM) images of (A) WO_3 nanorods, (B) WO_3/TiO_2 heterojunction film and (C) $WO_3/C/TiO_2$ film, with an intercalated carbon layer between the two semiconductor components. (D) Atomic force microscopy (AFM) image of the WO_3/TiO_2 heterojunction film.

2. Hard X-ray photoelectron spectroscopy analysis.

Hard X-ray photoelectron spectroscopy (HAXPES) measurements, to compliment the computational electronic processes at the WO_3/TiO_2 heterojunction interface, were carried out at Beamline I09 at Diamond Light Source. The valence band spectrum was measured for WO_3/TiO_2 heterojunction film and its individual components. It can be observed in Figure S2 that no differences in the binding energy of either Ti 2p or W 4d were detected between the heterojunction system and its corresponding single-component analogues (Figure S2A and S2B), indicating that the contact between WO_3 and TiO_2 does not alter the energy levels relative to the vacuum level on either side of the interface.

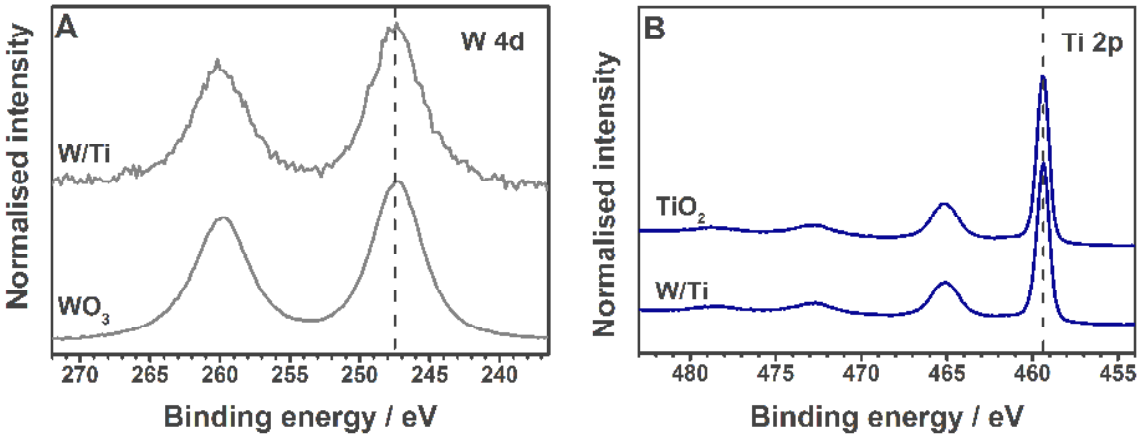

Figure S2. Hard X-ray photoelectron spectroscopy measurements of the WO_3/TiO_2 heterojunction film and the individual components, monoclinic WO_3 and anatase TiO_2. (A-B) Corresponding W $4d_{5/2}$ and Ti $2p_{3/2}$ peaks to show no detectable banding energy shifts between the samples.

3. Evaluation of photocatalytic properties of the films: the stearic acid test.

The photocatalytic activity of the films was evaluated during degradation of a model organic pollutant, octadecanoic (stearic) acid (95 %), under UVA irradiation. Stearic acid is highly stable under UV light (in the absence of an underlying effective photocatalyst) and its photo-degradation can be easily monitored for transparent samples via infrared spectroscopy following the weakening of typical C-H bands at 2598, 2923 and 2853 cm^{-1} (Figure S3A). A Perkin Elmer RX-I Fourier transform infrared (FTIR) spectrometer was used in our tests. The overall degradation reaction is:

$$CH_3(CH_2)_{16}CO_2H + 26O_2 \xrightarrow[h\nu \geq E_{bg}]{TiO_2} 18CO_2 + 18H_2O$$

In a typical test, a thin layer of stearic acid was deposited onto the film using a home-made dip coater from a 0.05 M stearic acid solution in chloroform. The integrated areas of the bands were periodically estimated upon UVA irradiation. The number of acid molecules degraded was estimated using a conversion factor (1 $cm^{-1} \equiv$ 9.7 x 10^{15} molecules cm^{-2}) from the literature.[4] The photoactivity rates were estimated from linear regression of the initial 30–

40 % degradation steps (zero-order kinetics) of the corresponding curves (Figure S3B). These results are typically expressed in terms of formal quantum efficiency, ξ (units, molecules photon^{-1}), defined as the number of molecules degraded per incident photon. The ξ values tend to underestimate the actual photocatalytic activity since not all incident photons are absorbed by the catalyst. In this estimation it is also assumed that all the incident photons had the same energy, *i.e.* 3.4 eV (365 nm). The light source was a blacklight-bulb lamp (BLB), 2×8 W (*Vilber-Lourmat*). The irradiance of the lamp (I= 3.15 mW cm^{-2}) was measured using a UVX radiometer (UVP).

It is worth comparing the photocatalytic efficiency of our WO_3/TiO_2 heterojunction with the enhancements observed for different heterojunction systems and chemically modified photocatalysts (Table S1). There is also an inherent difficulty to compare photocatalytic materials produced by different synthetic methods and research groups. This issue was bypassed here by comparing *enhancement factors* as estimated from activity ratios between the heterojunction (or doped) material and their corresponding best-performing single (or pure) component. For instance, the enhancement factor for the system reported by Chatchai *et al*.,[5] $WO_3/BiVO_4$, was calculated by taking the IPCE values at 365 nm for the heterojunction system and the most active single-component, $BiVO_4$, these values being ~ 71 % IPCE and ~ 8 % IPCE, respectively, and thus the estimated enhancement factor is ~ 9.

Table S1. Photocatalytic enhancement factors of representative heterojunction and doped materials reported in the literature. Synthetic method and photocatalytic test are included as reference. All photocatalytic materials were compared to their individual analogues.

Photocatalyst	Synthesis method	Test[a]	λ	Enhancement factor[b]	Refs.
WO_3/TiO_2	(AP)CVD	Stearic acid	UVA	14	**This work**
$WO_3/BiVO_4$	Spin coating	IPCE	365 nm	9	**5**
Cu_2O/TiO_2	Electrodeposition	IPCE	365 nm	8	**6**
$CaFe_2O_4$/ TaON	Electrophoretic deposition	IPCE	365 nm	8	**7**
V_2O_5/N,S-TiO_2	Solid state reaction route	IPCE	365 nm	7.5	**8**
CdS/TiO_2	Anodization/ Electrodeposition	IPCE	365 nm	7	**9**
Rutile/Anatase TiO_2	(AP)CVD	Stearic acid	UVA	7	**4**
Nano-Au:Ag:TiO_2	Sol-gel	Stearic acid	UVA	7	**10**
W:TiO_2	Sol-gel	Stearic acid	UVA	5	**10**
$TiO_2/SrTiO_3$	Hydrothermal synthesis	H_2 generation	UVC	4.5	**11**
MoS_2/CdS	Electrodeposition/ Chem Bath	IPCE	365 nm	4	**12**
Bi_2WO_6/ Ag/N–TiO_2	Spin coating	IPCE	365 nm	4	**13**
N:TiO_2	(AP)CVD	Stearic acid	UVA	3.5	**14**
TiO_2/WO_3	Electrospinning/ Thermal evaporation/ Thermal annealing	RhB	UVA	3	**15**
TiO_2/SnO_2	(PE)CVD	Phenol	UV	3	**16**
TiO_2/Cu_2O microgrid	Sol-gel/ Microsphere lithography	MB	UVA	2.5	**17**
TiO_2/SnO_2	Electrospinning	RhB	UV	2	**18**
$WO_3/BiVO_4$	Solvothermal/	IPCE	365 nm	2	**19**
TiO_2/In_2O_3	Spin coating Sol-gel	2-CP	UV	1.5	**20**
CeO_2/TiO_2	Colloidal templates/ ALD	MB	UVA	1.5	**21**
ZnO/TiO_2	Thermal sputtering/ Anodization	IPCE	365 nm	1.5	**22**
Bi_2S_3/WO_3	Solvothermal	IPCE	365 nm	1.5	**23**
Perovskite/ PCBM	Spin casting/ Thermal evaporation	IPCE	365 nm	1.5	**24**

[a]IPCE: incident photo-to-current efficiency in water splitting; RhB: Rhodamine B; MB: methylene blue; 2-CP: 2-chlorophenol. [b]Approximate enhancement factors estimated from activity ratios between the heterojunction (or chemically-modified/doped) material and the corresponding active analogue (or pure) component.

Sequential photocatalytic tests were carried out under UVA irradiation in order to investigate the photo-stability of our optimised WO_3/TiO_2 film. After each test the sample was cleaned using chloroform under stirring conditions in order to eliminate any trace of stearic acid and a new layer of the acid was deposited for subsequent testing. As clearly highlighted in Figure S3C, the photocatalytic performance of the WO_3/TiO_2 heterojunction film was reproducible, even a year after its synthesis (run 3). This observation is relevant since a crossover between number of cycles and reproducibility is often observed in thin film work due to delamination of the films.

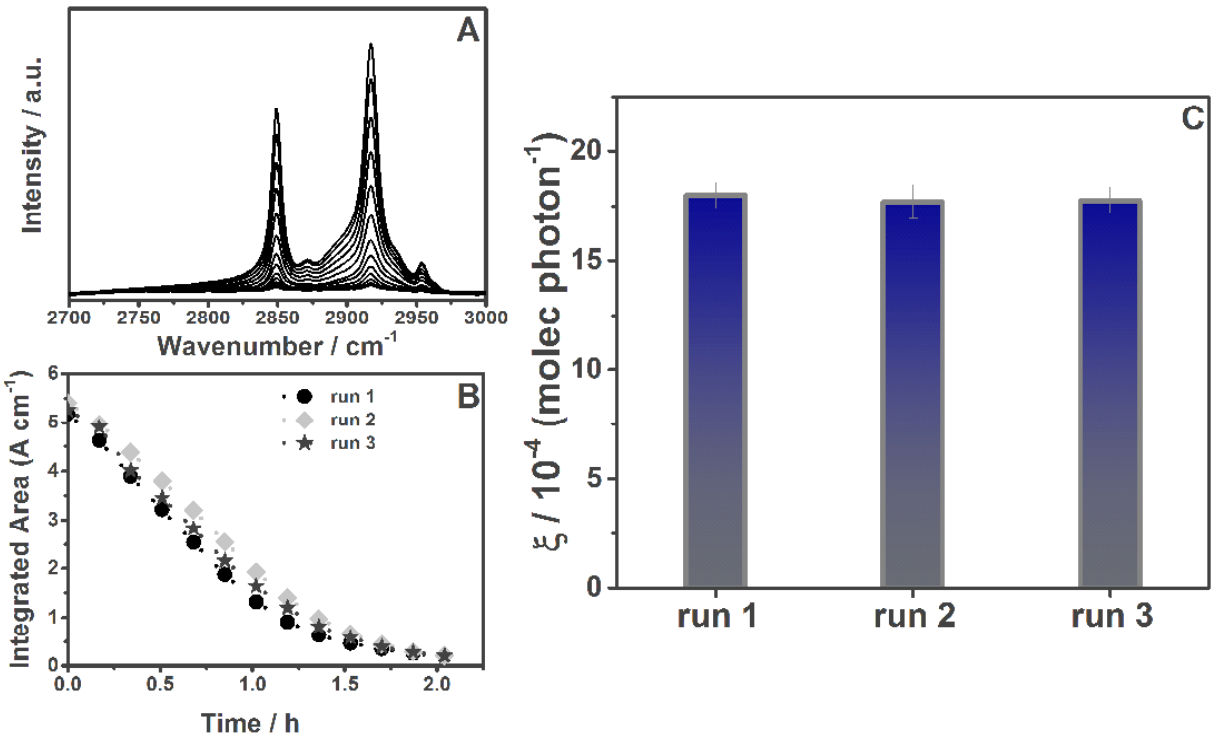

Figure S3. (A) IR spectra of stearic acid upon UVA illumination (I= 3.15 mW cm^{-2}) on a typical TiO_2/WO_3 heterojunction film. (B) Integrated areas obtained during sequential photocatalytic tests under UVA light and (C) corresponding formal quantum efficiencies. Run 3 was carried out a year after the synthesis of the WO_3/TiO_2 heterojunction film.

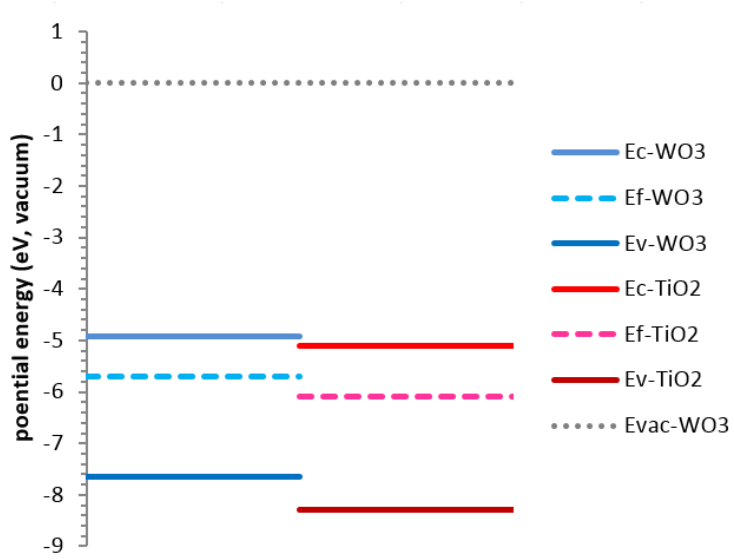

Figure S4. Dark, before Fermi level equilibration.

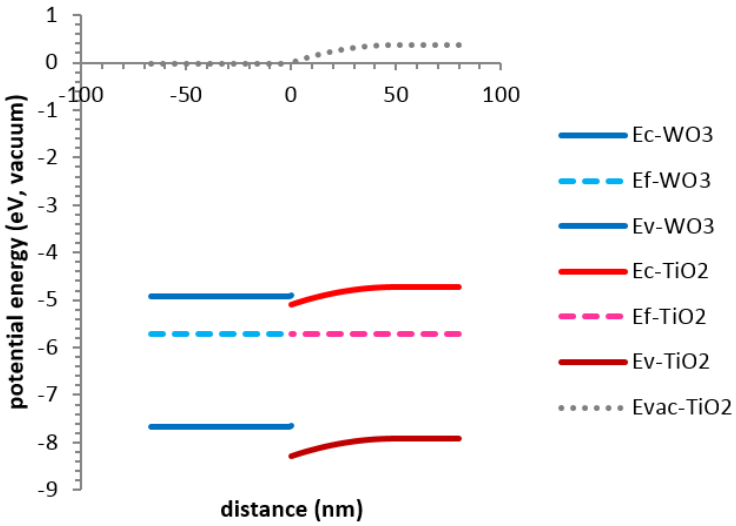

Figure S5. Dark, after Fermi level equilibration.

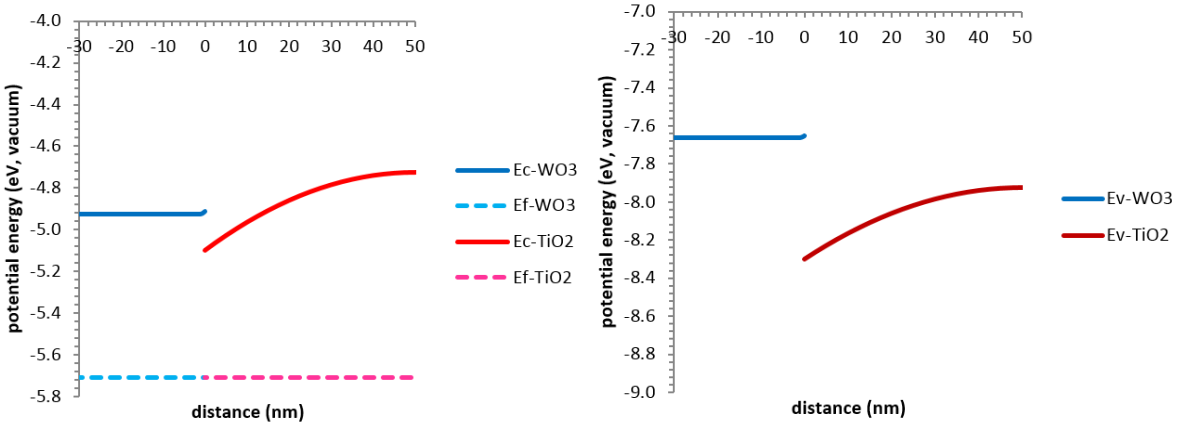

Figure S6. Close up of conduction and valence bands for dark after Fermi level equilibration.

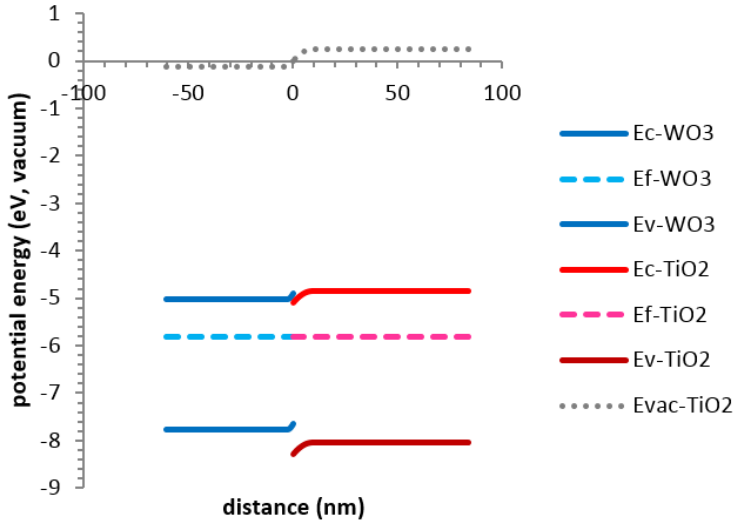

Figure S7. In the light, after Fermi level equilbration.

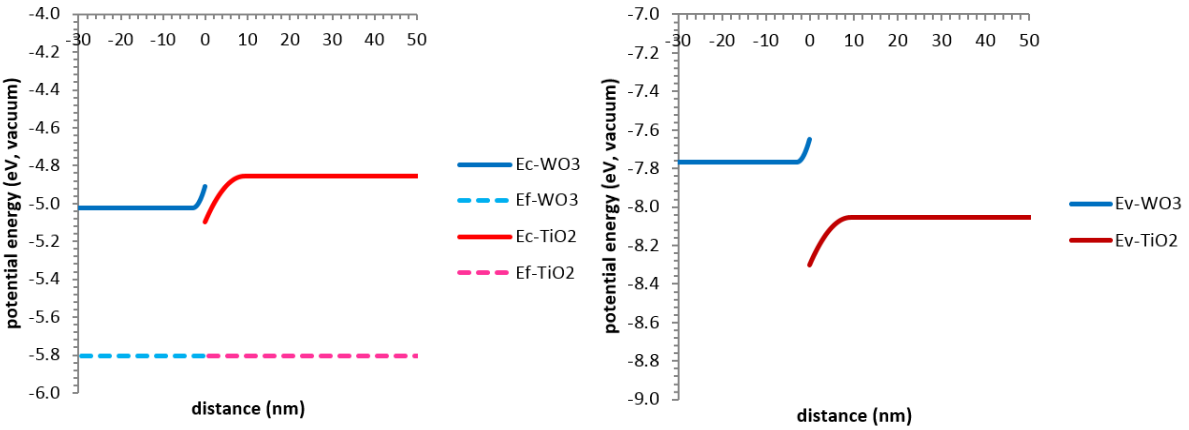

Figure S8. Close up of conduction and valence bands for in the light, after Fermi level equilibration.

The Fermi level positions and band bending in our WO_3/ TiO_2 heterojunction was modelled using a typical procedure (see Physics of Semiconductor Devices, 3rd Edition, by S . M. Sze and Kwok K. Ng - Chapter 2). Our HRTEM results showed that the TiO_2 and WO_3 layers were ~ 35 nm and ~ 60 nm wide. Charge carrier concentrations (n ~ 1 x 10^{19} cm^{-3} for TiO_2[25,26] and n ~ 2.5 x 10^{19} cm^{-3} for WO_3), di-electric constants (ε ~ 30 for anatase[27] and ε ~ 1000 for WO_3[28,29]) and conduction & valence band energies were taken from this work. The density of states was simulated using AFORS-HET v2.4 software.[30] The potential energies of the conduction and valence bands were taken from our computational studies, and the optical bandgaps from experiment.

4. References.

(1) M. Ling, C. Blackman, *Phys. Status Solidi C*. **2015**, *7*, 869.

(2) R. Quesada-Cabrera, C. Sotelo-Vazquez, J. C. Bear, J. A. Darr, I. P. Parkin, *Adv. Mater. Interfaces*, **2014**, *1*, 1400069.

(3) A. Mills, J. Wang, *J. Photchem. Photobiol. A Chem.*, **1998**, *118*, 53.

(4) A. Mills, J. Wang, *J. Photochem. Photobio. A Chem*., **2006**, *182*, 181.

(5) Chatchai, P.; Murakami, Y.; Kishioka, S.; Nosaka, A. Y.; Nosaka, Y. *Electrochim. Acta*. **2009**, *54*, 1147.

(6) Siripala, W.; Ivanovskaya, A.; Jaramillo, T. F.; Baeck, S-H.; McFarland, E. W. *Sol. Energ. Mat. Sol. Cells*. **2003**, *77*, 229.

(7) Kim, E. S.; Nishimura, N.; Magesh, G.; Kim, J. Y.; Jang, J.; Jun, H.; Kubota, J.; Domen, K.; Lee, J. S. *J. Am. Chem. Soc.* **2013**, *135*, 5375.

(8) Martha, S.; Das, D. P.; Biswal, N.; Parida, K. M. *J. Mater. Chem.* **2012**, *22*, 10695.

(9) Lai, Y.; Lin, Z.; Chen, Z.; Huang, J.; Lin, C. *Mater. Lett*. **2010**, *64*, 1309.

(10) Kafizas, A.; Kellici, S.; Darr, J. A; Parkin, I. P. *J. Photochem. Photobiol. A Chem.* **2009**, *204*, 183.

(11) Ng, B. J.; Xu, S.; Zhang, X.; Yang, H. Y.; Sun, D. D. *Adv. Funct. Mater*. **2010**, *20*, 4287.

(12) Liu, Y.; Yu, Y.; Zhang, W-D. *J. Phys. Chem. C*. **2013**, *117*, 12949.

(13) Xu, Q. C.; Ng, H.; Zhang, Y.; Chye, S.; Thatt, T.; Tan, Y. *Chem.Comm*. **2011**, *47*, 8641.

(14) Sotelo-Vazquez, C.; Quesada-Cabrera, R.; Darr, J. A.; Parkin, I. P. *J. Mater. Chem. A*. **2014**, *2*, 7082.

(15) Lu, B.; Li, X.; Wang, T.; Xie, E.; Xu, Z. *J. Mater. Chem. A*. **2013**, *1*, 3900.

(16) Cao, Y.; Zhang, X.; Yang, W.; Du, H.; Bai, Y.; Li, T.; Yao, J. *Chem. Mater*. **2000**, *12*, 3445.

(17) Zhang, J.; Zhu, H.; Zheng, S.; Pan, F.; Wang, T. *ACS Appl. Mater. Interfaces*. **2009**, *1* (10), 2111.

(18) Liu, Z.; Sun, D. D.; Guo, P.; Leckie, J. O. *Nano Lett*. **2007**, *7*, 1081.

(19) Su, J.; Guo, L.; Bao, N.; Grimes, C. A. *Nano Lett*. **2011**, 1928.

(20) Shchukin, D.; Poznyak, S.; Kulak, A.; Pichat, P. *J. Photochem. Photobiol. A Chem.* **2004**, *162*, 423.

(21) Alessandri, I.; Zucca, M.; Ferroni, M.; Bontempi, E.; Depero, L. E. *Small*. **2009**, *5*, 336.

(22) Shaheen, B. S.; Salem, H. G.; El-sayed, M. A.; Allam, N. K. *J. Phys. Chem. B*. **2013**, *117*, 18502.

(23) He, H.; Berglund, S. P.; Xiao, P.; Chemelewski, W. D.; Zhang, Y.; Mullins, C. B. *J. Mater. Chem. A*. **2013**, *1*, 12826.

(24) Jeng, J-Y.; Chiang, Y-F.; Lee, M-H.; Peng, S-R.; Guo, T-F.; Chen, P.; Wen, T-C. *Adv. Mater*. **2013**, *25*, 3727.

(25) van de Krol, R.; Goossens, A.; Schoonman, J. *J. Electrochem. Soc.* **1997**, *144*, 1723.

(26) Ankonina, G.; Chung, U.-J.; Chitu, A. M.; Komem, Y.; Rothschild, A. *Adv. Mater.* **2011**, *23*, 3266.

(27) Statemate, M.; Lazar, G.; Lazar, I. *Rom. J. Phys.* **2008**, *53*, 217.

(28) Hirose, T.; Furukawa, *Phys. Status Solidi Appl. Mater. Sci.* **2006**, *203*, 608.

(29) Ganbavle, V. V.; Agawane, G. L.; Moholkar, a. V.; Kim, J. H.; Rajpure, K. Y. *J. Mater. Eng. Perform.* **2014**, *23*, 1–10.

(30) Stangl, R.; Haschke, J.; Leendertz, C. *Numerical Simulation of Solar Cells and Solar Cell Characterization Methods: The Open-Source on Demand Program AFORS-HET, Version 2.4*; InTech e-book: "SolarEnergy," 2009.